Asociación Argentina
de Mecánica Computacional

Mecánica Computacional Vol XLII, pp. 1517-1526
A. Caggiano, G. Etse, P. Folino, M. Goldschmit, M. Pucheta, M. Storti (Eds.)
J. Álvarez Hostos, E.S. Esteban, G. Umbricht, C. Venier (Issue eds.)
Buenos Aires, November 11-14, 2025

A VERIFIED HYDRODYNAMIC–THERMAL BASELINE FOR WAX TRANSPORT AND DEPOSITION MODELING IN OIL PIPELINES

Ezequiel A. Krumrick[a], Ezequiel J. López[b] and Alberto G. Camacho[a]

[a]*Dpto. de Ingeniería Química, Universidad Tecnológica Nacional, Facultad Regional del Neuquén, Campamento Uno, 8318 Plaza Huincul, Argentina, http://www.frn.utn.edu.ar*

[b]*Instituto de Investigación en Tecnologías y Ciencias de la Ingeniería, Universidad Nacional del Comahue-CONICET, Buenos Aires 1400, 8300 Neuquén, Argentina, http://fainweb.uncoma.edu.ar*

Keywords: Wax deposition, flow assurance, heat transfer, mass transfer, CFD verification, OpenFOAM.

Abstract. A verified hydrodynamic-thermal baseline for laminar channel flow is established as a foundation for future wax-transport and wall-deposition modeling. The OpenFOAM 12 setup (meshing, numerics) is documented and a concise post-processing protocol is provided to ensure reproducibility. Convergence to a statistically steady regime is quantified via relative l2 norms of velocity and temperature referenced to t = 35 s. Local heat transfer is obtained from wall temperature gradients and bulk definitions, reporting streamwise Nusselt number as temporal medians with interquartile ranges over 30-35 s. The curve of the streamwise Nusselt number shows a short thermal-entry peak and approaches an asymptote at approximately 9.2 by a non-dimensional distance of about 13 hydraulic diameters. Latent effects and deposition kinetics are not included. The resulting dataset provides a verified reference upon which dissolved-wax transport and wall-layer growth will be coupled and validated.

ISSN: 2591-3522 DOI: 10.70567/mc.v42.ocsid8281

1 INTRODUCTION

Wax deposition remains a first-order flow-assurance risk: subcooling below the wax appearance temperature (WAT) narrows pipelines, escalates pressure drop, and forces costly mitigation (Burger et al., 1981; Azevedo and Teixeira, 2003; Aiyejina et al., 2011). Modeling spans from rapid heat-transfer analogies to interface-resolved Computational Fluid Dynamics (CFD), trading fidelity for complexity (Mehrotra et al., 2020; Magnini and Matar, 2019).

For single-phase oil, most reviews support *molecular diffusion*—modulated by wall cooling—as the leading driver, while shear and multiphase effects complicate predictions (Azevedo and Teixeira, 2003; Aiyejina et al., 2011; Kiyingi et al., 2022). Cold-finger and loop studies show thicker deposits at lower wall/bulk temperatures, reduced growth under higher shear, and strong time dependence due to gel aging and back-diffusion (Mahir et al., 2021; Singh et al., 2000, 2001).

This work establishes a transparent OpenFOAM 12 baseline for laminar channel-flow hydrodynamics and heat transfer, providing reproducible quantities of interest (QoIs) and verification metrics. The setup, numerics, and post-processing are documented; temporal stationarity is quantified; streamwise Nusselt number $|Nu_x|$ is reported as median + inter-quartile ranges (IQR); and grid effects are summarized via a compact Grid Convergence Index (GCI) analysis. These results complement prior heat-transfer studies (Krumrick and López, 2025; Banki et al., 2008; Magnini and Matar, 2019) and enable subsequent coupling of dissolved-wax transport and wall deposition.

2 MODEL AND METHODS

Simulations were performed with OpenFOAM 12 (Weller et al., 1998; Jasak, 1996).

2.1 Governing Transport

Incompressible momentum and energy are integrated with temperature- and shear-dependent viscosity $\mu(T, \dot{\gamma})$ in the momentum equations, while the energy equation uses constant density ρ, heat capacity c_p, and thermal conductivity k. Temperature acts as a passive scalar (no viscous or volumetric sources). Energy (conservative form) reads

$$\partial_t(\rho c_p T) + \nabla\cdot(\rho c_p \mathbf{U} T) = \nabla\cdot(k\nabla T),$$

Wax transport and deposition are deferred to follow-up work.

2.2 Domain, Mesh, and Boundary Conditions

A two-dimensional *symmetry half-channel* of height $h = 0.02$ m ($H = 2h$, hydraulic diameter $D_h = 2H = 0.08$ m) and length $L = 1.10$ m is used, with a single spanwise cell. Hexahedral meshes apply `simpleGrading` to cluster cells near the wall, as illustrated in Figure 1. Developed inlet profiles $U_{\mathrm{dev}}(y)$ and $T_{\mathrm{dev}}(y)$ are imposed using tabulated profiles, where y is the wall-normal coordinate; walls are isothermal at T_w; the outlet uses fixed (gauge) pressure $p\_rgh = 0.$ and an *advective (outflow) boundary condition* for T.

2.3 Discretization and Solvers

Second-order spatial schemes are used for gradients and diffusion; a bounded convection scheme is applied to T. Time stepping is constrained by the Courant–Friedrichs–Lewy (CFL, Co) and monitored against the Fourier number (Fo). Pressure–velocity coupling follows PIMPLE with fixed linear solvers and relaxation across all meshes.

2.4 Verification Metrics and Post-processing

Temporal stationarity is assessed by relative l_2 norms vs time, taking as reference time $t_{\mathrm{ref}} = 35$ s. Profiles at streamwise locations provide

$$U_b(x,t) = \frac{2}{H}\int_0^{H/2} U\,dy, \quad T_b(x,t) = \frac{\int_0^{H/2} UT\,dy}{\int_0^{H/2} U\,dy},$$

$$q_w(x,t) = -k\,(\partial T/\partial y)_w, \qquad Nu_x(x,t) = \frac{q_w D_h}{k\,[T_b - T_w]}.$$

We report $|Nu_x|$ as temporal medians with inter-quartile ranges over $t \in [30, 35]$ s. Grid effects are summarized by the observed order p, Richardson extrapolation, and GCI on a three-level mesh family. Details appear in Appendix A.

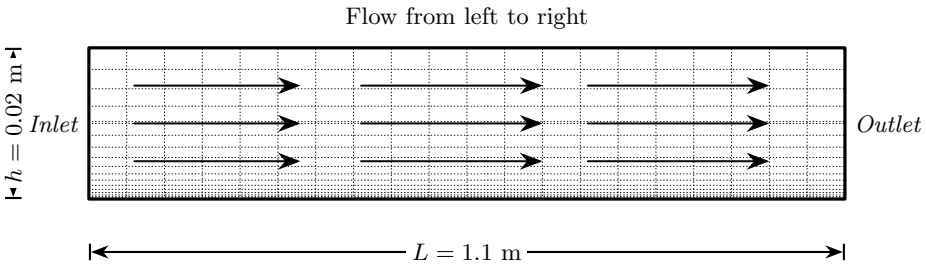

Figure 1: Computational domain (conceptual): 2D plane channel ($h = 0.02\,\mathrm{m}$, $L = 1.1\,\mathrm{m}$). Grading is applied to cluster cells toward the wall.

A single operating point was simulated to establish the verified baseline: $U_b = 0.15\ \mathrm{m\,s^{-1}}$, $D_h = 0.08$ m, $\rho = 845\ \mathrm{kg\,m^{-3}}$, $c_p = 2100\ \mathrm{J\,kg^{-1}\,K^{-1}}$, and $k = 0.13\ \mathrm{W\,m^{-1}\,K^{-1}}$. Viscosity is tabulated as $\mu(T, \dot\gamma)$ and evaluated at the wall shear rate $\dot\gamma_w = 6U_b/H$, yielding $\mu(T, \dot\gamma_w) = 118.2$ mPa s. The resulting Reynolds number based on the hydraulic diameter is $Re_{D_h} = \rho U_b D_h/\mu = 86$, confirming laminar flow. An additional elongated mesh ($L = 2.2$ m, 81×4456 cells) was used solely to verify the streamwise Nu_x and report $\mathrm{GCI}_{21}(x)$ and $p(x)$ in the asymptotic region; production results are reported on the fine mesh.

The viscosity is tabulated as $\mu(T, \dot\gamma)$ from Arias et al. (2024) and sampled at walls using $\dot\gamma_w = 6U_b/H$. To cover the full range of shear rates encountered in the simulations, the table was extended in $\dot\gamma$ by monotonic extrapolation and bilinear interpolation in $(T, \dot\gamma)$ was used throughout.

3 RESULTS AND VALIDATION

3.1 Temporal convergence

Figure 2 shows the decay of the relative l_2 norms of velocity and temperature using the field at $t_{\mathrm{ref}} = 35$ s as reference. Both variables cross the 10^{-3} threshold well before the averaging window; temperature at $t \approx 10$–11 s and velocity at $t \approx 17$–18 s. Accordingly, all heat-transfer results are reported as temporal medians with inter-quartile range (IQR) over $t \in [30, 35]$ s.

3.2 Local heat transfer

Figure 3 presents $|Nu_x|$ as a function of x/D_h, where symbols denote temporal medians and error bars the IQR over $t \in [30, 35]$ s. A mild thermal-entry peak appears near

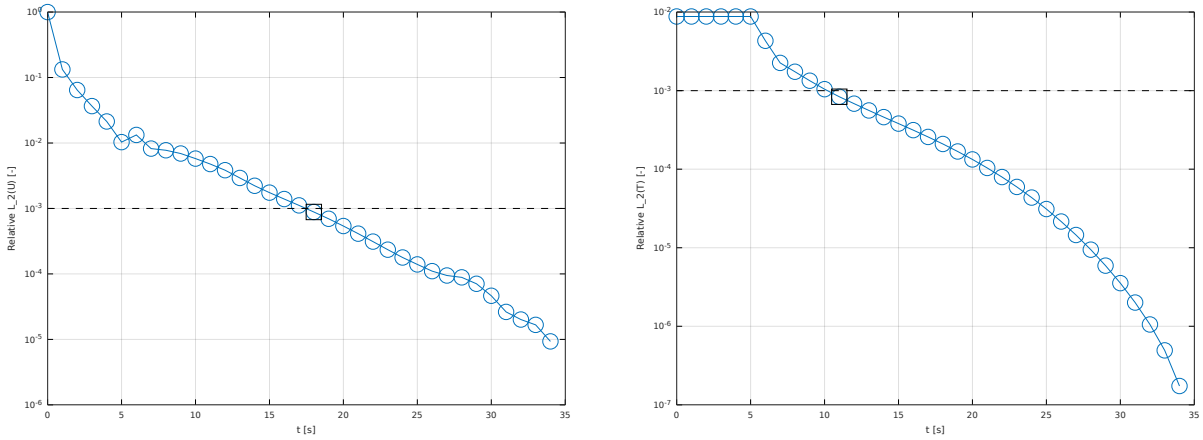

(a) Velocity relative l_2 vs time. (b) Thermal relative l_2 vs time.

Figure 2: Temporal convergence to *statistically steady* window used for averaging. Markers: ∘ relative l_2 norm; □ first crossing time t^* such that relative $l_2 \leq 10^{-3}$. Dashed line indicates the 10^{-3} threshold.

the inlet ($|Nu_x| \approx$ 10.0-10.1), followed by a gradual decrease towards an asymptotic level $|Nu_x| \approx$ 9.0-9.2 by $x/D_h \approx 13$. The classical fully-developed value $Nu_{fd} = 7.54$ for Newtonian, constant-property flow is not directly applicable here; property/rheology effects and the imposed wall temperature explain the higher asymptote observed.

In order to assess the streamwise evolution of local heat transfer, a laminar single-phase simulation was performed in a half-channel of length $L = 2.2$ m (hydraulic diameter $D_h = 0.08$ m). The computation was advanced for 100 s, which was sufficient for the local Nusselt statistics to reach stationarity. Figure 4 reports the time-averaged absolute local Nusselt number $|Nu_x|$ as a function of x/D_h together with its temporal variability at each station. After a short thermal-entry region, $|Nu_x|$ displays a shallow minimum and subsequently approaches a nearly constant downstream value, consistent with thermally developed conditions under wall cooling and temperature-dependent viscosity.

At a representative location, $|Nu_x|$ exhibits minor fluctuations around its median over $t \in [30, 35]$ s, with inter-quartile range well within plotting uncertainty and a coefficient of variation below $\sim 1\%$. This supports the use of temporal medians (with IQR) as robust summaries for $Nu_x(x/D_h)$.

3.3 Verification: Grid-Independence Metrics

Temporal verification uses relative l_2 norms referenced to $t_{\text{ref}} = 35$ s (Fig. 2); both velocity and temperature fall below 10^{-3} well before $t = 30$ s, which defines the statistically steady averaging window.

Spatial verification follows *Richardson extrapolation with the Grid Convergence Index (GCI)* (Richardson, 1911; Roache, 1998; Celik et al., 2008) on a three-level grid family (36×990, 54×1485, 81×2228) with geometric ratio $r = 1.5$ and safety factor $F_s = 1.25$. Position-dependent quantities are evaluated on coarse *x-stations* $x/D_h \in [0.125, 13.125]$; medium and fine values are linearly interpolated onto those *x-stations* to form triplets $\{Q_3, Q_2, Q_1\}(x)$. From these, the observed order $p(x)$, the Richardson-extrapolated estimate $Q_{\text{ext}}(x)$, and the fine–medium index $\text{GCI}_{21}(x)$ are obtained (details in the Appendix A).

Two complementary views are reported. First, streamwise curves of $\text{GCI}_{21}(x)$ for *wall-influenced QoIs* (Nu_x, q_w) show entrance peaks of 3.5–3.9%, a rapid decay, and a broad minimum around $x/D_h \approx$ 6–10, with medians (min–max) $\text{GCI}_{21}(Nu_x) \approx 2.14\%$ (1.02–3.84%) and

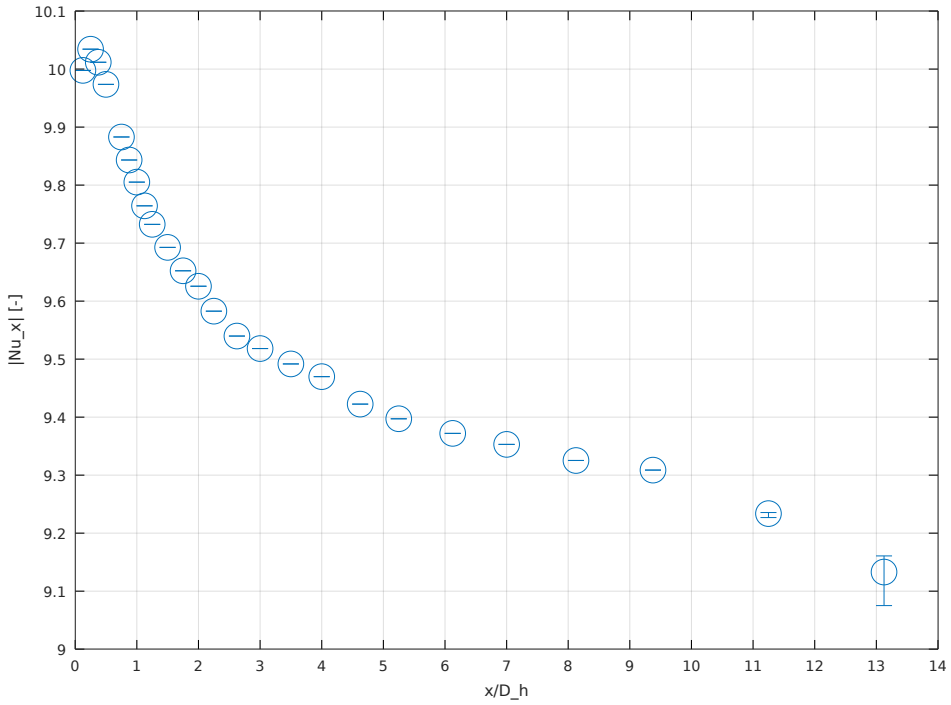

Figure 3: Local Nusselt number vs x/D_h; symbols show temporal medians and error bars the inter-quartile range over $t \in [30, 35]$ s.

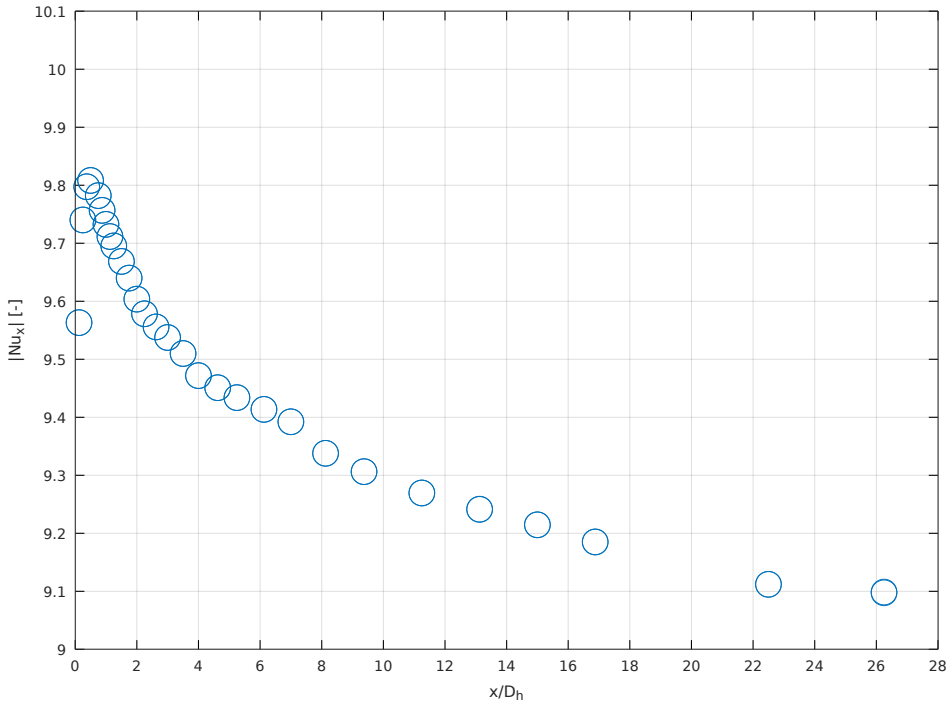

Figure 4: Instantaneous local Nusselt $|Nu_x|$ along the full domain ($L = 2.2$ m, $x/D_h \leq 27.5$); each marker denotes a single (x, t) sample within the final 1-s window $t \in [t_{\text{end}} - 1,\ t_{\text{end}}]$. The downstream clustering towards a plateau corroborates statistically steady conditions.

$\mathrm{GCI}_{21}(q_w) \approx 2.40\%$ (1.18–3.78%). Second, a probe point at $x/D_h = 13.125$ shows small indices and high observed order: for Nu_x, $p \approx 3.30$, $\mathrm{GCI}_{21} \approx 1.37\%$, $Q_1 = 9.133$, $Q_{\mathrm{ext}} = 9.233$; for q_w, $p \approx 2.71$, $\mathrm{GCI}_{21} \approx 2.15\%$, $Q_1 = -39.121\ \mathrm{W\,m^{-2}}$, $Q_{\mathrm{ext}} = -39.795\ \mathrm{W\,m^{-2}}$. Bulk metrics are effectively mesh-independent over the entire range, with $\mathrm{GCI}_{21}(U_b) \sim 7.5 \times 10^{-3}\%$ and $\mathrm{GCI}_{21}(T_b) \sim 7.2 \times 10^{-5}\%$.

Streamwise GCI statistics are summarized in Table 1. A single-point report at $x/D_h = 13.125$ is provided in Table 2.

QoI	N	$x_{\min}$	$x_{\max}$	**median** GCI_{21} **[%]**	min **[%]**	x@min	max **[%]**	x@max
Nu_x	25	0.125	13.125	2.143	1.018	8.125	3.842	0.375
q_w	25	0.125	13.125	2.401	1.181	9.375	3.778	0.375
U_b	25	0.125	13.125	0.007	0.000	6.125	0.015	0.250
T_b	25	0.125	13.125	0.000	0.000	0.375	0.083	9.375

Table 1: Summary of GCI_{21} along x/D_h for each QoI ($r = 1.5$, $F_s = 1.25$).

QoI	Q_1 **(fine)**	Q_{ext}	p	GCI_{21} **[%]**	**pattern**
Nu_x	9.133041	9.233133	3.295	1.370	monotonic
q_w	-39.121129	-39.794632	2.711	2.152	monotonic
U_b	0.149955	0.149955	9.262	0.000	osc/deg
T_b	282.635983	282.631819	2.935	0.002	osc/deg

Table 2: Single-point GCI at $x/D_h = 13.125$ for all QoIs ($r = 1.5$, $F_s = 1.25$).

3.4 Comparisons and Preliminary Validation

For constant-property laminar channel flow with isothermal walls, the fully developed value is $Nu_{fd} = 7.54$ (Shah and London, 1978). With non-isoviscous $\mu(T, \dot{\gamma})$ and an isothermal wall, the present cases exhibit higher downstream Nu_x, approaching an asymptote near 9.0-9.2 by $x/D_h \approx 13$ (Fig. 3). The entry-region peak and subsequent leveling are consistent with canonical thermal-entrance behavior. Quantitative statements are based on locations where mesh sensitivity is verified to be small (e.g., the probe point at $x/D_h = 13.125$); in the near-entrance region, trends are reported but not used as quantitative references due to larger, yet still moderate, GCI_{21}.

Streamwise grid sensitivity. The *wall-influenced QoIs* exhibit entrance peaks of $\mathrm{GCI}_{21} \approx 3.5$–$3.9\%$, followed by a rapid decay and a broad minimum around $x/D_h \approx 6$–10 where $\mathrm{GCI}_{21} \sim 1.2$–$1.7\%$. The wall heat flux q_w is consistently slightly more sensitive than Nu_x, yet both curves share the same trend, indicating error patterns consistent with the underlying physics (entrance effects then downstream leveling). The observed order $p(x)$ rises from $\sim$ 2.3–2.7 near the inlet to $\sim$ 3.0–3.3 downstream, with a peak for Nu_x of $\sim$ 3.6–3.7 at $x/D_h \approx 8$. A probe point in the asymptotic region ($x/D_h = 13.125$) shows low indices and high p, supporting its use for reporting $(p, \mathrm{GCI}_{21}, Q_1, Q_{\mathrm{ext}})$.

4 DISCUSSION

Steep near-wall thermal gradients combined with the sensitivity of $\mu(T, \dot{\gamma})$ increase numerical stiffness in the entrance region; monotone flux limiters then stabilize those layers at the

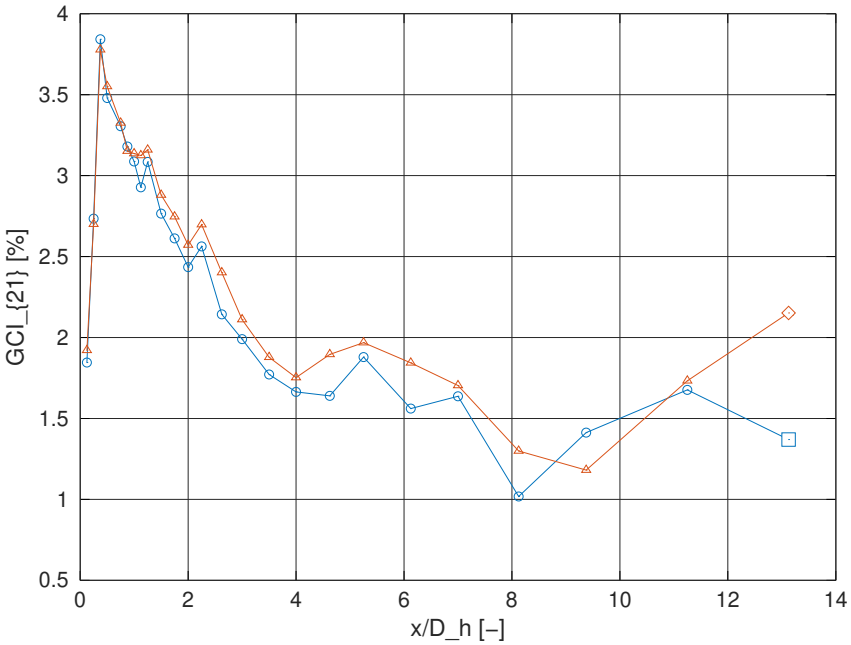

Figure 5: Streamwise $\mathrm{GCI}_{21}(x)$ for *wall-influenced QoIs*. Entrance peaks (3.5–3.9%), rapid decay, and a broad minimum around $x/D_h \approx 6$–10; q_w is slightly more sensitive than Nu_x. Curves: $\circ$ Nu_x; $\triangle$ q_w. Symbols: $\square$ Nu_x at the reporting station; $\diamond$ q_w at the reporting station.

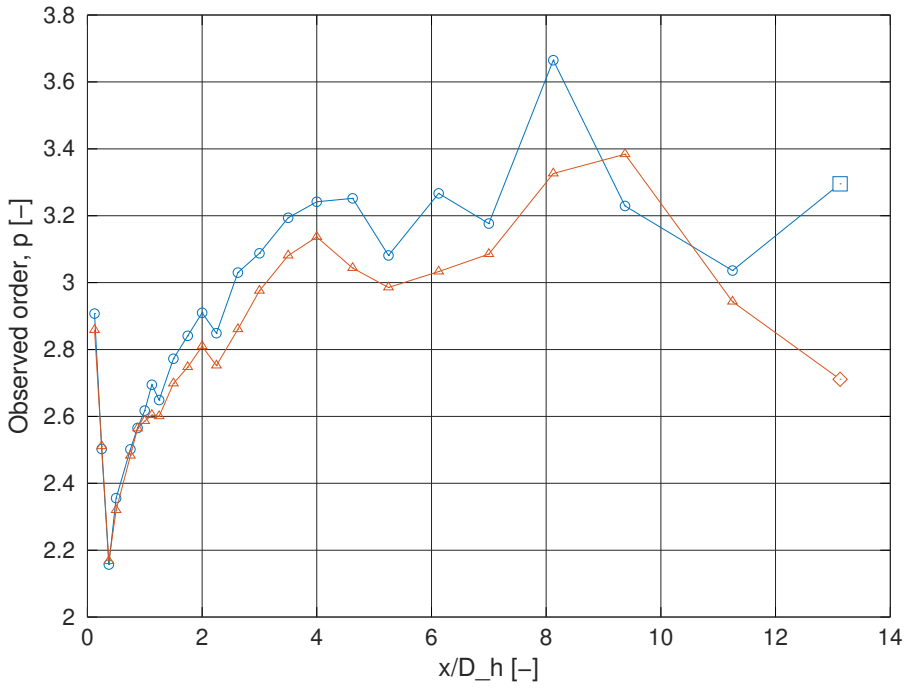

Figure 6: Observed order $p(x)$: rises from ∼2.3–2.7 near the inlet to ∼3.0–3.3 downstream; a local maximum for Nu_x near $x/D_h \approx 8$. Curves: $\circ$ Nu_x; $\triangle$ q_w. Symbols: $\square$ Nu_x at the reporting station; $\diamond$ q_w at the reporting station.

expense of local accuracy, which explains the larger GCI_{21} and the lower observed orders near the inlet, and the recovery to $p > 2$ downstream as gradients weaken (Sweby, 1984; Harten, 1983; LeVeque, 2002; Moukalled et al., 2016). A fourth grid level together with mild near-wall refinement is expected to further reduce the entrance-peak GCI_{21} and the downstream indices, without altering the observed asymptotic $|Nu_x|$. These verification results provide the baseline confidence required before coupling dissolved-wax transport and wall-deposition kinetics, for which accurate wall gradients directly govern interfacial fluxes.

5 CONCLUSIONS AND FUTURE WORK

Conclusions. A reproducible hydrodynamic–thermal baseline was established in OpenFOAM 12 for laminar channel flow with temperature- and shear-dependent viscosity. Temporal stationarity enables reporting medians with inter-quartile ranges over a statistically steady window. Grid verification on a three-level family ($r = 1.5$) shows moderate entrance sensitivity and small downstream indices: at $x/D_h = 13.125$, Nu_x and q_w converge monotonically with $\mathrm{GCI}_{21} \approx 1.37\%$ and 2.15%, respectively. Bulk metrics U_b and T_b are effectively mesh-independent (indices below $10^{-4}\%$).

Future work. (i) Introduce liquid-phase (VoF-weighted) dissolved-wax transport with a temperature-driven wall flux and verify global mass conservation between transported and deposited wax; (ii) incorporate latent-heat effects in the energy equation and a wall-attached deposit layer with shear/aging-dependent removal; (iii) reduce local GCI_{21} by adding a fourth grid level and targeted near-wall/interface refinement; (iv) extend to turbulent inflow conditions and to interface-resolved benchmark cases to broaden validation.

ACKNOWLEDGEMENTS

This work has received financial support from Consejo Nacional de Investigaciones Científicas y Técnicas (CONICET, Argentina), Universidad Nacional del Comahue (UNCo, Argentina, grant 04/I-251), Agencia Nacional de Promoción de la Investigación, el Desarrollo Tecnológico y la Innovación (Agencia I+D+i, Argentina, grants PICT-2021-I-A-00651 and PICT-2021-I-A-00582), Universidad Tecnológica Nacional Facultad Regional del Neuquén (UTN FRN, Argentina), and was performed with the Free Software Foundation /GNU-Project resources such as GNU-LinuxOS and Doxygen, as well as other Open Source resources as the OpenFOAM Foundation, LaTeX, and Octave.

A GRID CONVERGENCE INDEX (GCI)

Details of the error model, Richardson extrapolation and the GCI computation follow Roache (1998); Celik et al. (2008), including the treatment of monotonic vs. oscillatory convergence and the reporting conventions for GCI_{21}.

A three-level grid family $\{\Delta_f, \Delta_m, \Delta_c\}$ was employed with refinement ratio $r = \Delta_m/\Delta_f = \Delta_c/\Delta_m > 1$. For a quantity of interest Q, the observed order p was estimated by

$$p = \frac{\ln\left(\dfrac{Q_c - Q_m}{Q_m - Q_f}\right)}{\ln(r)}.$$

The Richardson-extrapolated value is

$$Q_{\mathrm{ext}} = Q_f + \frac{Q_f - Q_m}{r^p - 1}.$$

The fine-grid GCI reads

$$\mathrm{GCI}_{\mathrm{fine}} = F_s \frac{|Q_f - Q_m|}{|Q_f|} \frac{1}{r^p - 1},$$

with safety factor $F_s = 1.25$. The same procedure was applied to pressure drop Δp, outlet bulk temperature $T_{b,\mathrm{out}}$, and the local Nu_x at $x/D_h = 13.125$; Δp and $T_{b,\mathrm{out}}$ are mesh-independent within numerical round-off, consistent with Tables 1–2.

REFERENCES

Aiyejina A., Chakrabarti D.P., Pilgrim A., and Sastry M.K.S. Wax formation in oil pipelines: A critical review. *International Journal of Multiphase Flow*, 37(7):671–694, 2011. http://doi.org/10.1016/j.ijmultiphaseflow.2011.02.007.

Arias M.L., D'Adamo J.G.L., Novosad M.N., Raffo P.A., Burbridge H.P., and Artana G.O. An in-depth experimental study of wax deposition in pipelines. *International Journal of Aerospace and Mechanical Engineering*, 18(4):144–152, 2024. ISSN 2393-8609.

Azevedo L.F.A. and Teixeira A.M. A critical review of the modeling of wax deposition mechanisms. *Petroleum Science and Technology*, 21(3-4):393–408, 2003. http://doi.org/10.1081/LFT-120018528.

Banki R., Hoteit H., and Firoozabadi A. Mathematical formulation and numerical modeling of wax deposition in pipelines from enthalpy–porosity approach and irreversible thermodynamics. *International Journal of Heat and Mass Transfer*, 51(13–14):3387–3398, 2008. http://doi.org/10.1016/j.ijheatmasstransfer.2007.11.012.

Burger E.D., Perkins T.K., and Striegler J.H. Studies of wax deposition in the trans alaska pipeline. *Journal of Petroleum Technology*, 33(6):1075–1086, 1981. http://doi.org/10.2118/8788-PA.

Celik I.M., Ghia U., Roache P.J., Freitas C.J., Coleman H., and Raad P.E. Procedure for estimation and reporting of uncertainty due to discretization in CFD applications. *Journal of Fluids Engineering*, 130(7):078001, 2008. http://doi.org/10.1115/1.2960953.

Harten A. High resolution schemes for hyperbolic conservation laws. *Journal of Computational Physics*, 49(3):357–393, 1983. http://doi.org/10.1016/0021-9991(83)90136-5.

Jasak H. *Error Analysis and Estimation for the Finite Volume Method with Applications to Fluid Flows*. Phd thesis, Imperial College of Science, Technology and Medicine, University of London, 1996.

Kiyingi W., Guo J.X., Xiong R.Y., Su L., Yang X.H., and Zhang S.L. Crude oil wax: A review on formation, experimentation, prediction, and remediation techniques. *Petroleum Science*, 19(5):2343–2357, 2022. http://doi.org/10.1016/j.petsci.2022.08.008.

Krumrick E.A. and López E.J. Numerical simulation of heat transfer in a flow assurance loop. In *X Congreso de Matemática Aplicada, Computacional e Industrial (MACI 2025)*. AMCA, Córdoba, Argentina, 2025. Sesión S25.

LeVeque R.J. *Finite Volume Methods for Hyperbolic Problems*. Cambridge University Press, Cambridge, 2002. ISBN 9780521009249.

Magnini M. and Matar O.K. Fundamental study of wax deposition in crude oil flows in a pipeline via interface-resolved numerical simulations. *Industrial & Engineering Chemistry Research*, 58:21797–21816, 2019. http://doi.org/10.1021/acs.iecr.9b05250.

Mahir L.H.A., Lee J., Fogler H.S., and Larson R.G. An experimentally validated heat and mass transfer model for wax deposition from flowing oil onto a cold surface. *AIChE Journal*, 67:e17063, 2021. http://doi.org/10.1002/aic.17063.

Mehrotra A.K., Ehsani S., Haj-Shafiei S., and Kasumu A.S. A review of heat-transfer mechanism for solid deposition from "waxy" or paraffinic mixtures. *Canadian Journal of Chemical Engineering*, 98(12):2463–2488, 2020. http://doi.org/10.1002/cjce.23829.

Moukalled F., Mangani L., and Darwish M. *The Finite Volume Method in Computational Fluid Dynamics*, volume 113 of *Fluid Mechanics and Its Applications*. Springer, Cham, 2016. ISBN 978-3-319-16873-9. http://doi.org/10.1007/978-3-319-16874-6.

Richardson L.F. The approximate arithmetical solution by finite differences of physical problems involving differential equations, with an application to the stresses in a masonry dam. *Philosophical Transactions of the Royal Society A*, 210:307–357, 1911.

Roache P.J. *Verification and Validation in Computational Science and Engineering*. Hermosa Publishers, Albuquerque, NM, 1998. ISBN 9780913478080.

Shah R.K. and London A.L. *Laminar Flow Forced Convection in Ducts*. Academic Press, New York, 1978.

Singh P., Venkatesan R., Fogler H.S., and Nagarajan N. Formation and aging of incipient thin film wax–oil gels. *AIChE Journal*, 46(5):1059–1074, 2000. http://doi.org/10.1002/aic.690460517.

Singh P., Venkatesan R., Fogler H.S., and Nagarajan N.R. Morphological evolution of thick wax deposits during aging. *AIChE Journal*, 47(1):6–18, 2001. http://doi.org/10.1002/aic.690470103.

Sweby P.K. High resolution schemes using flux limiters for hyperbolic conservation laws. *SIAM Journal on Numerical Analysis*, 21(5):995–1011, 1984. http://doi.org/10.1137/0721062.

Weller H.G., Tabor G., Jasak H., and Fureby C. A tensorial approach to computational continuum mechanics using object-oriented techniques. *Computers in Physics*, 12(6):620–631, 1998. http://doi.org/10.1063/1.168744.